

ARTICLE

Open Access

Controlled growth of a graphdiyne-Prussian blue analog heterostructure for efficient ammonia production

Yaqi Gao¹, Huimin Liu¹, Zhiqiang Zheng¹, Xiaoyu Luan¹, Yurui Xue¹ and Yuliang Li^{1,2,3}

Abstract

Selective and efficient ammonia (NH₃) production using an electrocatalytic nitrate reduction reaction (ECNtRR) under ambient conditions provides a green and promising alternative to the traditional energy-intensive Haber–Bosch process. The challenge is in design and controlled syntheses of efficient electrocatalysts with high selectivities, high NH₃ yield rates (Y_{NH₃}) and long-term stabilities. Here, a freestanding three-dimensional graphdiyne-hollowed FeCoNi Prussian blue analog electrode (*h*-FeCoNi PBA@GDY) with highly selective and active interfaces was synthesized by in situ growth of a GDY layer on the surface of *h*-FeCoNi PBA and used for the ECNtRR in alkaline solution at ambient temperatures and pressures. The experimental results demonstrated that the uniquely incomplete charge transfer between metal atoms and GDY effectively enhanced the intrinsic activity and increased the number of active sites of the electrocatalyst and promoted fast redox switching and high-density charge transport at the interface, which resulted in high selectivity, activity and stability for the ECNtRR. The results indicated that the electrocatalyst showed a Faraday efficiency (FE) of 95.1% with a Y_{NH₃} of 1015.5 μmol h⁻¹ cm⁻² and excellent stability.

Ammonia (NH₃) is an important and basic material and plays a critical role in fertilizers for agricultural production. It is also an ideal carbon-free energy carrier with a high hydrogen energy density, a highly anticipated clean energy source for hydrogen conversion in the future and a key route to achieving carbon neutrality^{1–9}. The Haber–Bosch process is currently the primary method used for industrial production of NH₃. However, this process requires high temperatures (>400 °C) and pressures (>150 bar) to activate the chemically inert nitrogen (N₂; N≡N) and force the reaction of N₂ with H₂ to produce NH₃; this results in a serious waste of resources, energy inefficiency, and pollution. Many researchers have

attempted to develop an environmentally friendly, energy efficient, and pollution-free method for NH₃ production at ambient temperatures and pressures. Recently, NH₃ production using an electrocatalytic nitrogen reduction reaction (ECNRR) under ambient conditions has been considered an attractive alternative to the Haber–Bosch process^{3–11}. Practical application of the ECNRR for mass NH₃ production is still a great challenge because of limited N₂ solubility in water, the high splitting energy of the N≡N bond and the competing hydrogen evolution reaction (HER). These scientific issues are limitations and result in low selectivity and NH₃ yield rate (Y_{NH₃}). There is no doubt that finding more reactive nitrogen sources with higher water solubility to replace N₂ would be an effective way to solve these issues and achieve large-scale NH₃ production.

Among nitrogen-containing molecules, nitrate (NO₃⁻) is an important alternative to N₂ as a nitrogen source due to its unlimited solubility in water, much lower activation energy than N₂, and easy adsorption on the surfaces of

Correspondence: Yurui Xue (yrxue@sdu.edu.cn) or Yuliang Li (ylli@iccas.ac.cn)

¹Shandong Provincial Key Laboratory for Science of Material Creation and Energy Conversion, Science Center for Material Creation and Energy Conversion, School of Chemistry and Chemical Engineering, Shandong University, Jinan 250100, P. R. China

²CAS Key Laboratory of Organic Solids, Institute of Chemistry, Chinese Academy of Sciences, Beijing 100190, P. R. China

Full list of author information is available at the end of the article

© The Author(s) 2023



Open Access This article is licensed under a Creative Commons Attribution 4.0 International License, which permits use, sharing, adaptation, distribution and reproduction in any medium or format, as long as you give appropriate credit to the original author(s) and the source, provide a link to the Creative Commons license, and indicate if changes were made. The images or other third party material in this article are included in the article's Creative Commons license, unless indicated otherwise in a credit line to the material. If material is not included in the article's Creative Commons license and your intended use is not permitted by statutory regulation or exceeds the permitted use, you will need to obtain permission directly from the copyright holder. To view a copy of this license, visit <http://creativecommons.org/licenses/by/4.0/>.

catalysts, which are beneficial in alleviating mass transfer barriers in the electrolytic process and improving the overall performance for NH_3 production. In addition, nitrate is one of the most serious water pollutants and is harmful to human health and the environment¹¹. Significantly, the electrocatalytic nitrate reduction reaction (ECNtRR) would provide a promising and economical approach to ammonia production with advantages such as high efficiency, low energy consumption, and pollution-free operation at ambient temperatures and pressures, and it would simultaneously consume the nitrates in industrial wastewater, polluted groundwater and surface water and maintain the balance of the nitrogen cycle^{12–14}. However, the ECNtRR is a complex eight-electron and nine-proton process during which it is easy to produce byproducts, and this results in lower reaction selectivity and efficiency. It is imperative to develop new electrocatalysts with high selectivity and high NH_3 yields (Y_{NH_3}) under ambient conditions.

Recently, a number of electrocatalysts have been reported for ECNtRRs run under ambient conditions^{12–17}. However, there is still a large gap between the performance of these catalysts and practical commercialization. Heterojunction catalysts are advanced catalytic systems that have undergone rapid development in recent years, and they provide a direction for catalyst development in the future^{18–28}. Heterojunction electrocatalysts have high selectivity, high activity and stability, which is the key to developing high-performance ECNtRR electrocatalysts. The d -orbital electrons enable electron transfer into the lowest vacant molecular orbital of nitrate²⁹. The catalysts, including metal elements with highly occupied d -orbitals and open d -orbital shells (e.g., Fe, Co, Ni, etc.) have exhibited superior catalytic performance. Prussian blue analogs (PBAs) have attracted considerable interest for application in catalysis and energy conversion because of their easy syntheses, adjustable structures, and promising electrochemical properties³⁰. However, their low conductivities and limited structural stabilities limit application in the field of catalysis.

Combining traditional materials with carbon materials to form heterogeneous interface structures is a very promising way to obtain new catalysts with targeted reaction selectivity, activity and stability³¹. Among all reported carbon materials, graphdiyne (GDY) is the first sp - and sp^2 -cohybridized two-dimensional carbon material, and it exhibits many unique and distinguishing properties, such as a large highly π -conjugated network, abundant carbon chemical bonds, extremely uneven surface charge, natural pores and band gap, high intrinsic charge carrier mobility, high electrical conductivity, and excellent stability^{14,19,27,28,32–45}. Compared with traditional carbon materials, GDY has an unparalleled advantage in that it can be grown controllably on the surface of any substrate under low temperatures and

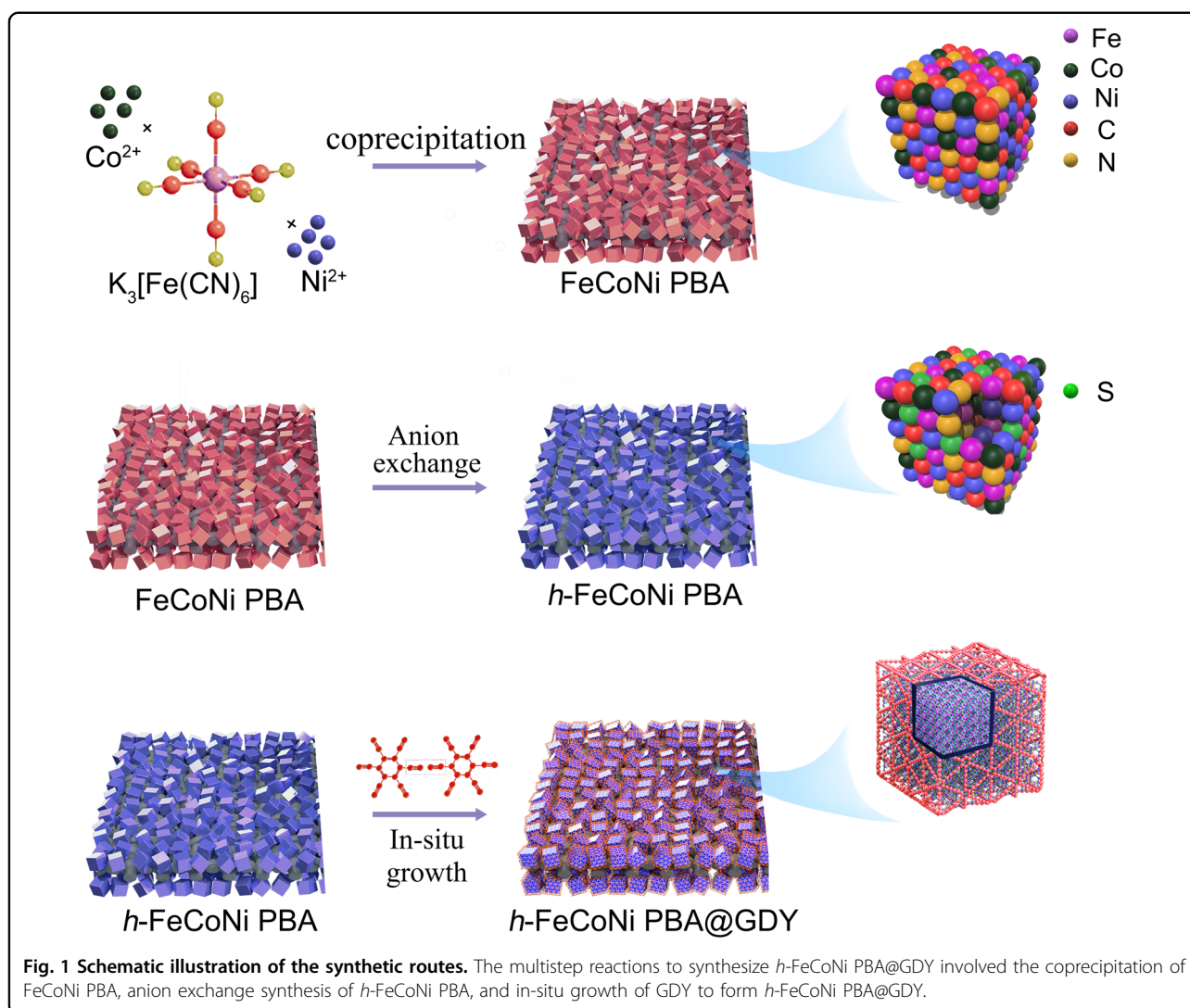
mild conditions. Benefiting from these unique properties, a number of GDY-based materials have been fabricated and have shown potential in various fields, including catalysis, energy conversion and storage, batteries, solar cells, intelligence, and life sciences^{5,9,46–61}. These advantages of GDY make it an ideal material for constructing of interface structures with a significant numbers of active sites, facilitated charge transfer, enhanced catalytic activity and long-term stability.

Herein, we demonstrate facile fabrication of GDY-based multi-interface heterostructures via in situ growth of GDY films on the surfaces of hollowed FeCoNi PBA nanocubes (h -FeCoNi PBA@GDY). The experimental results demonstrate that incomplete charge transfer between metal atoms and GDY significantly improved the charge transfer ability of h -FeCoNi PBA@GDY, enhanced the conductivity, and increased the number of active sites, which resulted in excellent ECNtRR performance with a Y_{NH_3} of $1015.5 \mu\text{mol h}^{-1} \text{cm}^{-2}$ and a FE of 95.1% with low overpotentials. These values compare favorably to previously reported values. Furthermore, h -FeCoNi PBA@GDY exhibits long-term stability over 14 continuous cycles.

Results and discussion

As shown in Fig. 1, h -FeCoNi PBA@GDY was prepared via a facile three-step method. Typically, the FeCoNi PBA nanocubes were first synthesized via coprecipitation by using carbon cloth (CC) as the growth substrate (step I). Then, the freshly prepared FeCoNi PBA nanocubes were added to sodium sulfide solution and converted into hollowed FeCoNi PBA nanoboxes (h -FeCoNi PBA) through an anion-exchange-etching process (step II). Finally, h -FeCoNi PBA@GDY (mass loading: 0.12 mg cm^{-2}) was obtained by in situ growth of a GDY layer on the h -FeCoNi PBA surface.

Field-emission scanning electron microscopy (SEM) images showed that the CC substrate had a 3D porous architecture woven from the carbon fiber with a smooth (Fig. 2a, b) and hydrophobic surface (Fig. 2c). After the coprecipitation reaction, FeCoNi PBA nanocubes with smooth surfaces were uniformly and densely grown on the surface of the CC (Fig. 2d–f). The cubic morphology of the FeCoNi PBA was well maintained after treatment with the sodium sulfide solution (Fig. 2g–i). The as-synthesized samples were next used as substrates for in situ growth of the GDY. Remarkably, Fig. 2j–l shows that h -FeCoNi PBA@GDY had a cubic morphology but a rougher surface, which could be attributed to in situ growth of the GDY. These morphological characteristics effectively enlarged the active surface area and therefore increased the number of active sites, which enhance the electrocatalytic activity. Energy-dispersive spectroscopy (EDS) mapping results confirmed the presence and uniform dispersion of Fe, Co, Ni, C, N and S elements in h -FeCoNi PBA@GDY (Fig. 2m).

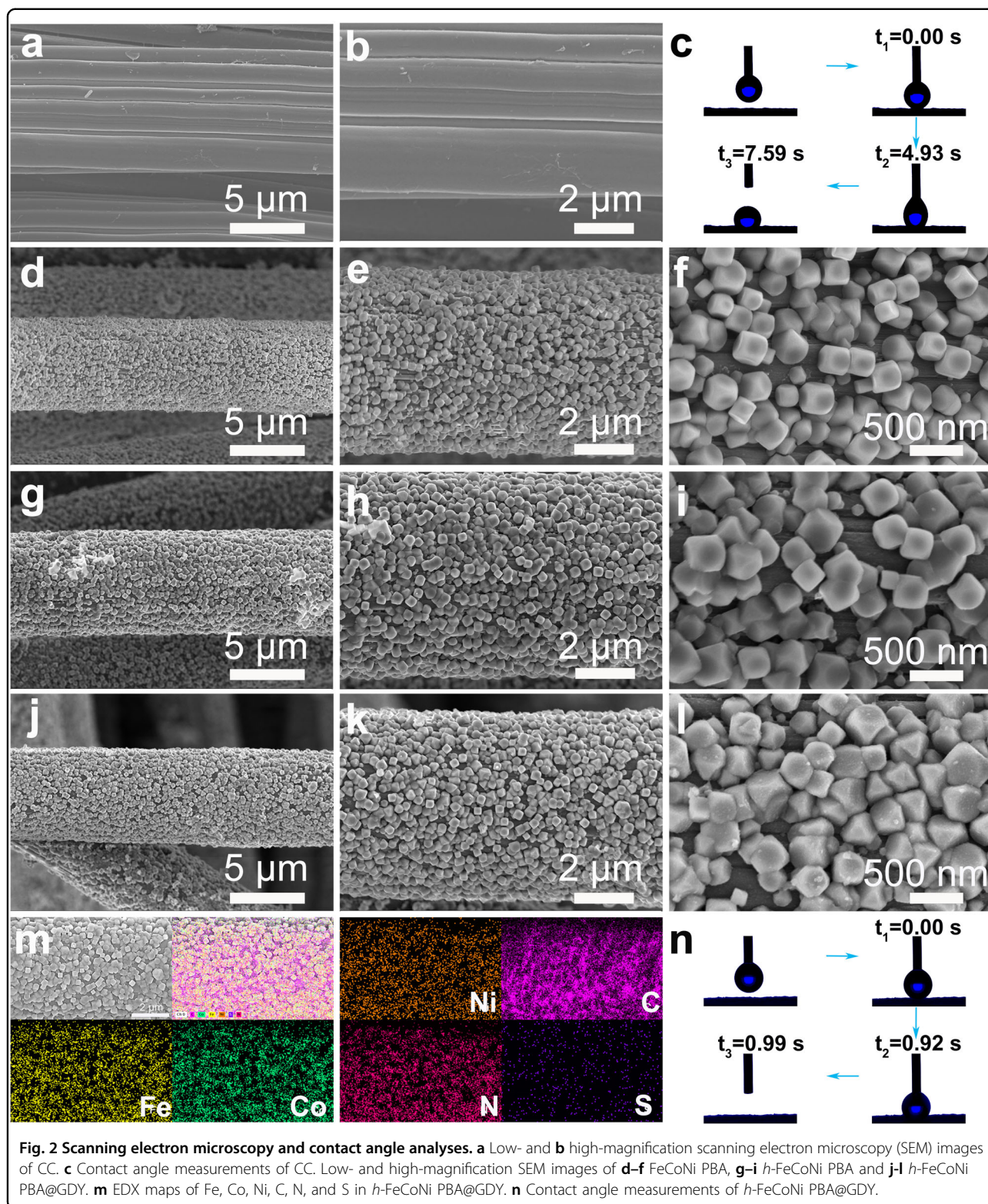


Contact angle measurements revealed that *h*-FeCoNi PBA@GDY has a superhydrophilic surface (Fig. 2n), which improved the mass/ion transport capability and reduced contact resistance, thereby improving the overall electrocatalytic performance.

Transmission electron microscopy (TEM), high-resolution TEM (HRTEM) and scanning TEM (STEM) were used to study the morphologies of the samples. The STEM (Fig. 3a) image revealed a solid cubic morphology and smooth surface for FeCoNi PBA. The HRTEM image (Fig. 3b) showed the monocrystalline nature of FeCoNi PBA with a lattice spacing of 0.517 nm. Elemental mapping images showed the uniform distribution of Fe, Co, Ni, C and N throughout the FeCoNi PBA nanocubes (Fig. 3c). In contrast to FeCoNi PBA, *h*-FeCoNi PBA contains distinct hollow interiors, which also confirmed the success of the anion-exchange-etching process (Fig. 3d). Interestingly, *h*-FeCoNi PBA showed two lattice spacings of 0.560 nm and

0.242/0.289 nm (Fig. 3e), which correspond to the structures of PBA and metal sulfides. In addition, elemental mapping images for a single *h*-FeCoNi PBA nanobox show the inner distributions of Co and S and the outermost distributions of Fe, Co, Ni, C and N, along with the presence of less S (Fig. 3f). Subsequently, a uniform GDY layer was successfully grown on the surface of *h*-FeCoNi PBA (Fig. 3g, i). The intimate interactions between the *h*-FeCoNi PBA and GDY were clearly observed (Fig. 3h). The HRTEM images (Fig. 3j–m) of *h*-FeCoNi PBA@GDY showed lattice fringes with distances of 0.363 nm, 0.279 and 0.242 nm, and 0.521 nm, which were ascribed to GDY, metal sulfides, and PBA, respectively.

Raman spectroscopy and X-ray photoelectron spectroscopy (XPS) were used to further investigate the elemental compositions and chemical states of the samples. Figure 4a shows the Raman spectra of GDY and *h*-FeCoNi PBA@GDY. GDY exhibited four typical peaks for the D



band (1380 cm^{-1}), G band (1599 cm^{-1}) and vibrations of the conjugated diynes (1950 and 2152 cm^{-1}). Compared with GDY, an additional peak at 1023 cm^{-1} corresponding

to the *h*-FeCoNi PBA species was observed, which demonstrated the successful synthesis of the *h*-FeCoNi PBA@GDY heterostructure. The relative intensity ratio for

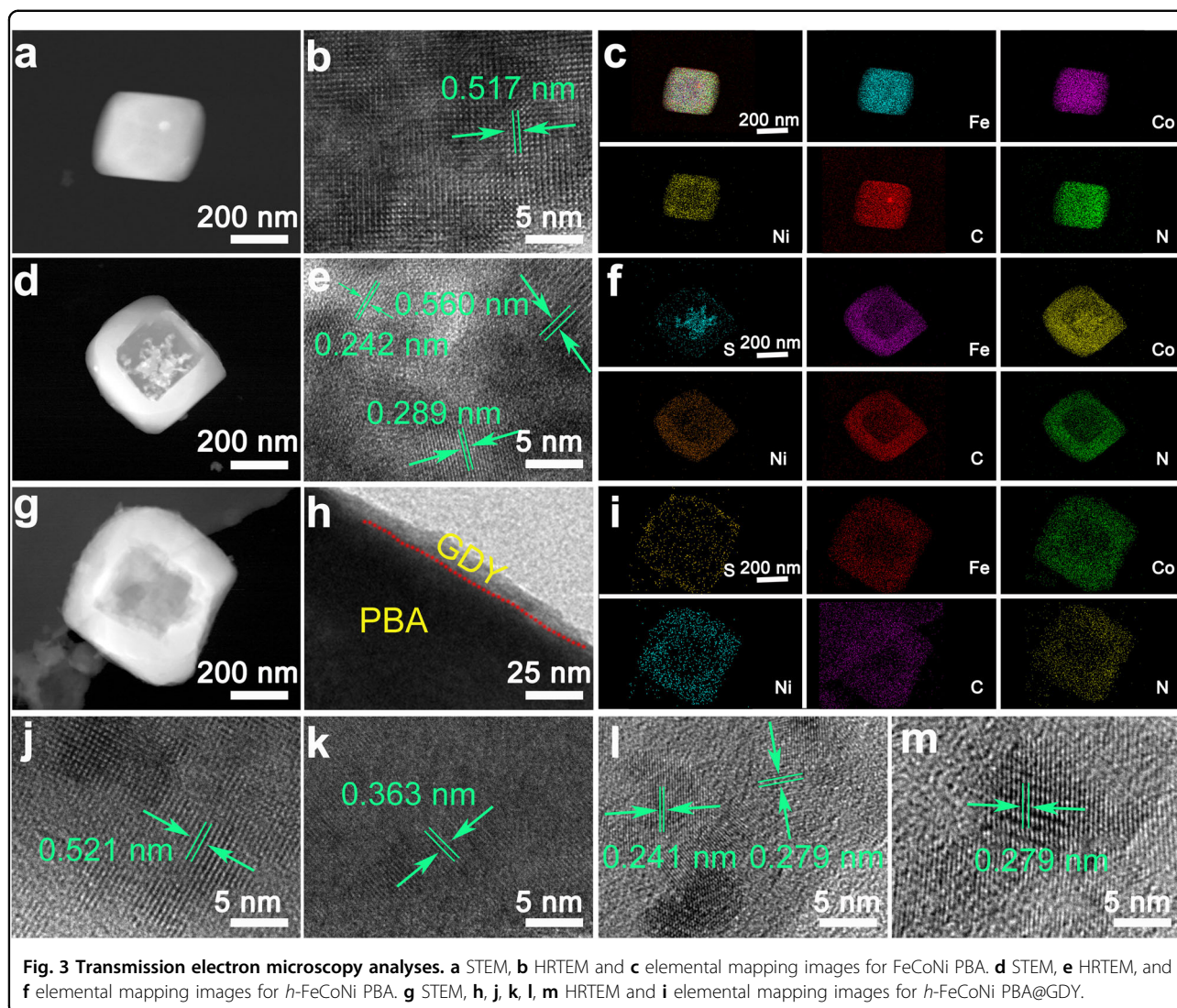
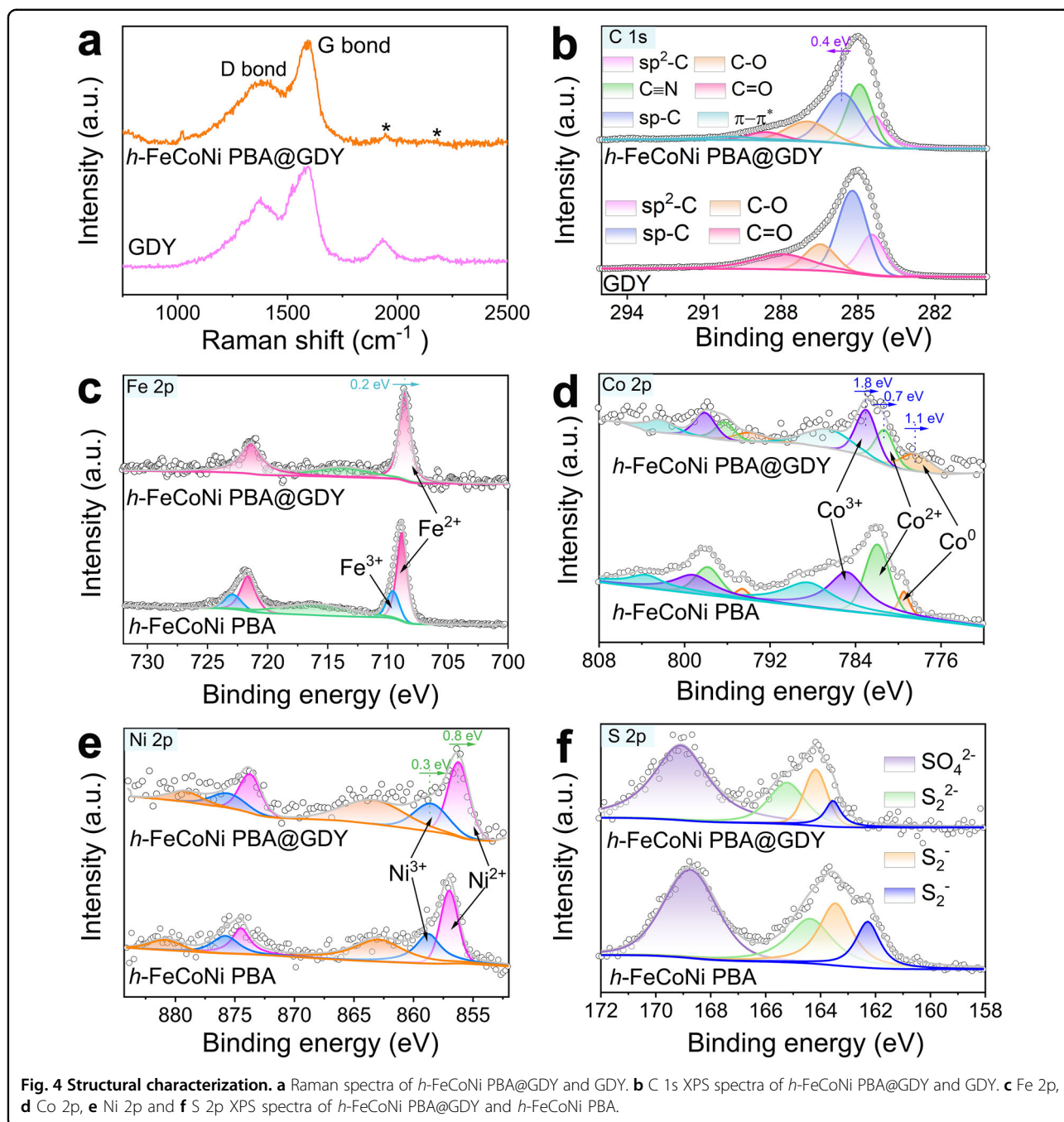


Fig. 3 Transmission electron microscopy analyses. **a** STEM, **b** HRTEM and **c** elemental mapping images for FeCoNi PBA. **d** STEM, **e** HRTEM, and **f** elemental mapping images for *h*-FeCoNi PBA. **g** STEM, **h**, **j**, **k**, **l**, **m** HRTEM and **i** elemental mapping images for *h*-FeCoNi PBA@GDY.

the D and G bands (I_D/I_G) reflects the relative number of defects in the sample⁶². *h*-FeCoNi PBA@GDY had a higher I_D/I_G value (0.86) than pure GDY (0.67), indicating the presence of more defects in *h*-FeCoNi PBA@GDY, which would promote electron delocalization and accelerate charge transfer⁶³. The XPS survey spectrum (Fig. S1) confirmed the presence of Fe, Co, Ni, C, N, and S in the samples. The C 1s XPS spectrum of GDY (Fig. 4b) exhibited four peaks at 284.0, 284.6, 286.1, and 288.1 eV, which corresponded to $-C=C-$ (sp^2-C), $-C\equiv C-$ ($sp-C$), $-C-O$, and $-C=O$ species, respectively. For *h*-FeCoNi PBA@GDY, the C 1s XPS spectrum was deconvoluted into six peaks for $-C=C-$ (284.3 eV), $C\equiv N$ (284.9 eV), $-C\equiv C-$ (285.6 eV), $-C-O$ (287.0 eV), $-C=O$ (288.6 eV) and $\pi-\pi^*$ (289.9 eV). The presence of a peak for the $\pi-\pi^*$ transition reflected the interaction between GDY and *h*-FeCoNi PBA. The area ratio for the $sp^2-C/sp-C$ peaks of *h*-FeCoNi PBA@GDY was 0.5, which

is consistent with that of GDY, indicating that the structure of GDY remained intact in the heterostructure and demonstrating the robustness of the GDY structure. The sp^2-C peak shifted by 0.25 eV to a higher binding energy than the pristine GDY, which indicated charge transfer from GDY to the *h*-FeCoNi PBA species. The Fe 2p XPS spectrum (Fig. 4c) indicated the coexistence of the Fe^{2+}/Fe^{3+} redox couple in *h*-FeCoNi PBA and the presence of only Fe^{2+} in *h*-FeCoNi PBA@GDY. This result confirmed charge transfer from the GDY to the Fe species in *h*-FeCoNi PBA@GDY. As shown in Fig. 4d, the Co 2p XPS spectrum of *h*-FeCoNi PBA@GDY displayed two spin-orbit triplets at 783.0, 798.1, 781.3, 796.3, 778.4, and 793.9 eV as well as two satellite peaks at 786.6 and 802.4 eV. The triplets are attributable to Co^{3+} , Co^{2+} , and Co^0 species. Compared with those for pure *h*-FeCoNi PBA, the Co 2p_{1/2} and 2p_{3/2} peaks for *h*-FeCoNi PBA@GDY shifted to lower binding energies, which confirmed the

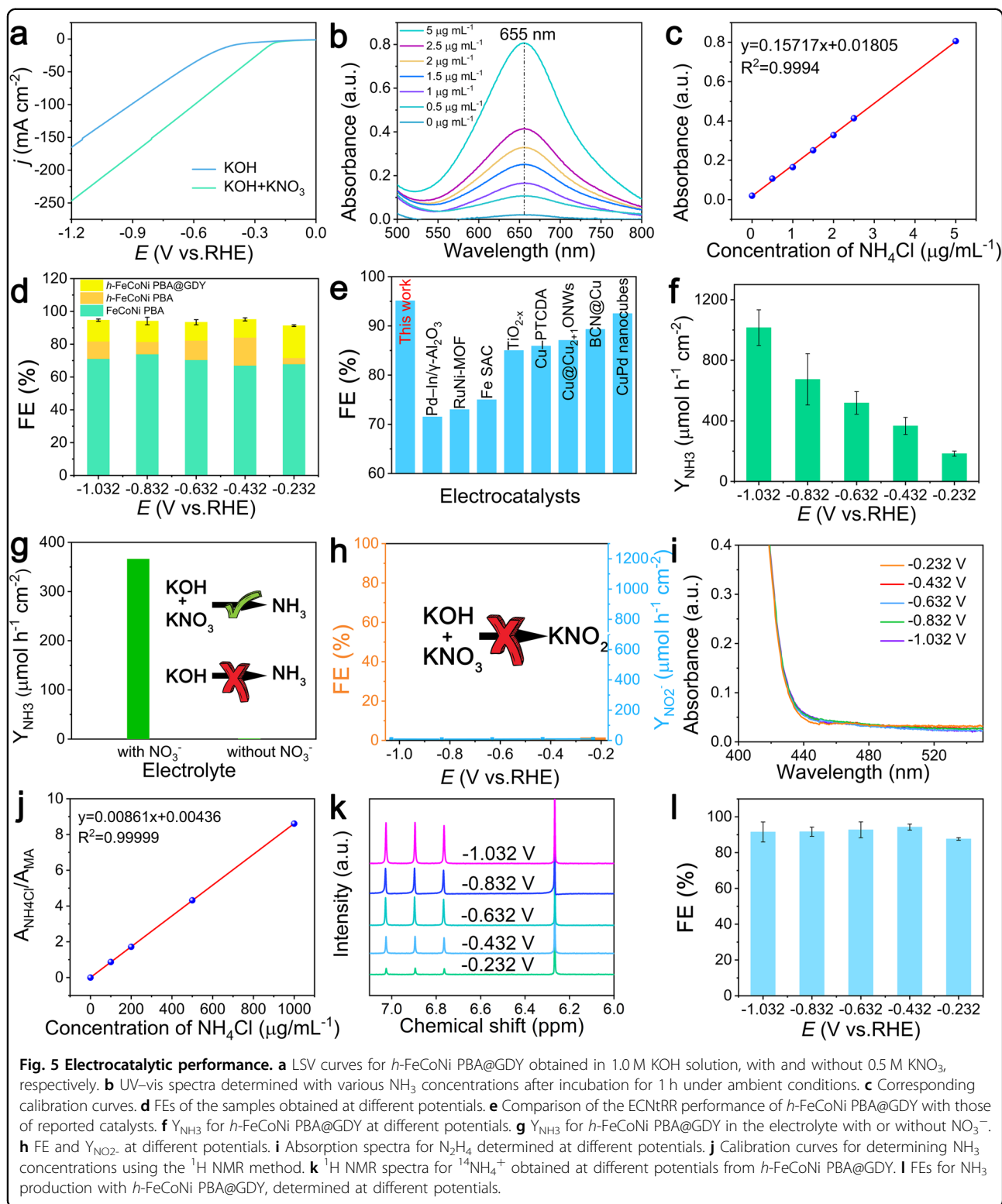


charge transfer from GDY to Co species in *h*-FeCoNi PBA@GDY. The high-resolution Ni 2p XPS spectrum for *h*-FeCoNi PBA@GDY (Fig. 4e) exhibited two $3d_{3/2}/3d_{1/2}$ doublet peaks at 856.2/858.5 and 873.7/875.6 eV, which were ascribed to Ni^{2+} and Ni^{3+} species and confirmed the coexistence of Ni^{2+} and Ni^{3+} species. The Ni 2p binding energy also exhibited a negative shift relative to that of pure *h*-FeCoNi PBA. Figure 4f shows the S 2p XPS spectra of *h*-FeCoNi PBA@GDY and *h*-FeCoNi PBA. In the S 2p spectrum, the peaks at 163.55, 164.18, and 165.22 eV were

assigned to terminal S_2^{2-} , bridging S_2^{2-} and apical S^{2-} of *h*-FeCoNi@GDY. These results demonstrated the enhanced charge transfer from GDY to the metal species in *h*-FeCoNi PBA@GDY, which enhanced the intrinsic activity.

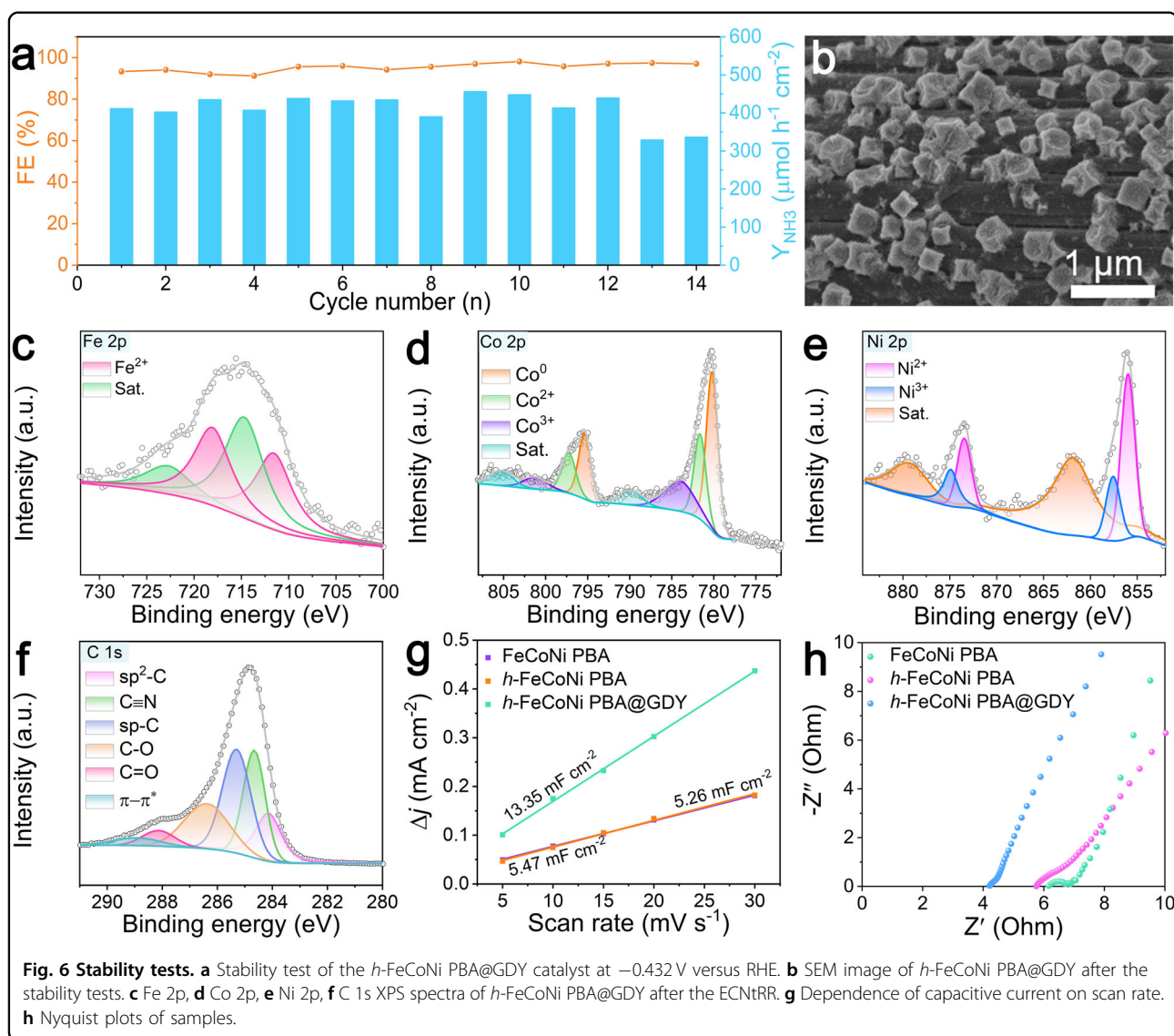
Electrocatalytic nitrate reduction performance

The ECNtRR catalytic capabilities of the samples were studied in a customized H-type cell under alkaline conditions at a constant potential for 1 h. Figure 5a shows the



linear sweep voltammetry (LSV) curves for *h*-FeCoNi PBA@GDY, which were recorded in 0.5 M KNO₃ + 1.0 M KOH and 1.0 M KOH electrolyte solutions, respectively. *h*-FeCoNi PBA@GDY exhibited larger current densities

in 0.5 M KNO₃ + 1.0 M KOH than in 1.0 M KOH at the same applied potentials, which indicated that the ECNtRR was facilitated in the presence of nitrate. Ultraviolet-visible (UV-Vis) spectrophotometry and nuclear magnetic



resonance spectroscopy (NMR) were employed to detect the synthesized NH_3 . The UV-Vis adsorption spectrum for pure NH_4Cl in KOH solution (Fig. 5b) and the associated calibration curves (Fig. 5c) were first determined. As shown in Fig. 5d, *h*-FeCoNi PBA@GDY displayed high FEs in excess of 90% over a wide potential window ranging from -0.232 V to -1.032 V versus RHE; the highest FE of 95.1% was seen at -0.432 V vs. RHE and exceeded those for most of the reported electrocatalysts (Fig. 5e; Table S1). Figure 5f shows that the Y_{NH_3} for *h*-FeCoNi PBA@GDY increased with increasing applied potential and reached a maximum Y_{NH_3} of $1015.5 \mu\text{mol h}^{-1} \text{cm}^{-2}$ at -1.032 V vs. RHE. A series of control experiments were next conducted to determine the N source of the NH_3 product. As shown in Fig. 5g, large amounts of NH_3 were produced in the presence of nitrates, while negligible NH_3 was detected in the absence of nitrates. This confirmed

that the NH_3 product resulted from electroreduction of nitrate. Previous reports demonstrated that the rate-limiting step for ECNtRR is the sluggish NO_3^- -to- NO_2^- conversion process^{64,65}. Almost no NO_2^- (Figs. 5h, S2) or N_2H_4 (Figs. 5i, S3 and S4) were detected during the ECNtRR process, which indicated the high selectivity of *h*-FeCoNi PBA@GDY for the ECNtRR. The electrolytes remaining after the ECNtRR were also tested with proton nuclear magnetic resonance spectroscopy (^1H NMR, Figs. 5j–l, S5). As shown in Fig. 5k, three peaks corresponding to $^{14}\text{NH}_4^+$ clearly indicated its presence in the electrolyte after 1 h of electrolysis. The experimental results showed that the FE values determined by ^1H NMR (Fig. 5l) were consistent with those determined by UV-Vis spectroscopy, which confirmed the precision and accuracy of quantitative concentration determinations for the generated NH_3 .

The long-term stability of *h*-FeCoNi PBA@GDY was determined with continuous cycling tests. As shown in Fig. 6a, the Y_{NH_3} and FE for the *h*-FeCoNi PBA@GDY sample showed slight fluctuations but remained stable over 14 cycles under ambient conditions, indicating the excellent stability of *h*-FeCoNi PBA@GDY during operation of the ECNtRR. In addition, the SEM image (Fig. 6b) and XPS data (Figs. 6c–f and S6) revealed that the morphology and structure of *h*-FeCoNi PBA@GDY were well maintained after the stability tests, which confirmed the robust structural stability of the catalyst. Compared with freshly prepared *h*-FeCoNi PBA@GDY, the Fe 2p, Co 2p, and Ni 2p binding energies of the used samples exhibited obvious shifts, which indicated that significant charge transfer occurred during electrocatalysis. In addition, the $\text{Co}^{3+}/\text{Co}^{2+}$ and $\text{Ni}^{3+}/\text{Ni}^{2+}$ intensity ratios decreased from 1.49 to 0.76 and from 0.58 to 0.49, respectively. To gain deep insight into the origins of the excellent catalytic performance, electrochemically active surface area (ECSA) and electrochemical impedance spectra (EIS) measurements were carried out. The ESCAs proportional to the double-layer capacitance (C_{dl}) were estimated by using a CV method (Fig. S7). *h*-FeCoNi PBA@GDY showed a capacitance of 13.35 mF cm^{-2} , larger than those of FeCoNi PBA (5.26 mF cm^{-2}) and *h*-FeCoNi PBA (5.47 mF cm^{-2}) (Fig. 6g). This implied that *h*-FeCoNi PBA@GDY has the largest number of active sites, which increases electrocatalytic activity. The Nyquist plots (Figs. 6h, S8 and Table S2) were fitted to a R(QR)(QR) equivalent-circuit model consisting of solution resistance (R_s) and charge transfer resistance (R_{ct}). *h*-FeCoNi PBA@GDY showed the smallest R_s and R_{ct} ($R_s = 4.23 \Omega$, $R_{\text{ct}} = 0.11 \Omega$), which indicated improved charge transfer kinetics and the highest conductivity. These factors determined the intrinsic electrochemical properties of *h*-FeCoNi PBA@GDY.

Conclusion

In summary, we demonstrated a rational and facile strategy for controlled synthesis of *h*-FeCoNi PBA@GDY heterostructures for selective and efficient catalysis of the ECNtRR in alkaline solution at ambient temperature and pressure. Our results demonstrated that incomplete charge transfer between metal atoms and GDY at the interface greatly improved the charge transfer ability and conductivity of the electrocatalyst, leading to formation of more active sites and therefore greatly increasing the NH_3 production efficiency. When used for the ECNtRR, the electrocatalyst exhibited high catalytic performance with an FE of 95.1% and Y_{NH_3} of $1015.5 \mu\text{mol h}^{-1} \text{ cm}^{-2}$ at low overpotentials. This work provides a promising approach for design and fabrication of efficient and inexpensive electrocatalysts supporting ammonia synthesis under ambient conditions and future applications in the renewable energy field.

Acknowledgements

We acknowledge the support from the National Natural Science Foundation of China (21790050, 21790051, and 22021002), the National Key Research and Development Project of China (2018YFA0703501), the Key Program of the Chinese Academy of Sciences (XDPB13), the Taishan Scholars Youth Expert Program of Shandong Province (tsqn201909050), and the Natural Science Foundation of Shandong Province (ZR2020ZD38, ZR2021JQ07).

Author details

¹Shandong Provincial Key Laboratory for Science of Material Creation and Energy Conversion, Science Center for Material Creation and Energy Conversion, School of Chemistry and Chemical Engineering, Shandong University, Jinan 250100, P. R. China. ²CAS Key Laboratory of Organic Solids, Institute of Chemistry, Chinese Academy of Sciences, Beijing 100190, P. R. China. ³University of Chinese Academy of Sciences, Beijing 100049, P. R. China

Author contributions

Y.G. synthesized the catalysts, carried out the experiments, analyzed the data, and wrote the draft. H.L., X.L. and Z.Z. provided help during the experiments. Y.X. and Y.L. conceived the idea, designed the research, and critically revised the manuscript.

Data availability

The data that support the findings detailed in this study are available in the article and its Supplementary Information or from the corresponding authors upon reasonable request.

Competing interests

The authors declare no competing interests.

Publisher's note

Springer Nature remains neutral with regard to jurisdictional claims in published maps and institutional affiliations.

Supplementary information The online version contains supplementary material available at <https://doi.org/10.1038/s41427-022-00439-8>.

Received: 22 July 2022 Revised: 2 October 2022 Accepted: 5 October 2022.
Published online: 31 March 2023

References

- Erisman, J. W., Sutton, M. A., Galloway, J., Klimont, Z. & Winiwarter, W. How a century of ammonia synthesis changed the world. *Nat. Geosci.* **1**, 363–369 (2008).
- Ye, T. N. et al. Vacancy-enabled N_2 activation for ammonia synthesis on a Ni-loaded catalyst. *Nature* **583**, 391–395 (2020).
- Hui, L. et al. Highly efficient and selective generation of ammonia and hydrogen on a graphdiyne-based catalyst. *J. Am. Chem. Soc.* **141**, 10677–10683 (2019).
- Fang, Y. et al. Graphdiyne interface engineering: highly active and selective ammonia synthesis. *Angew. Chem. Int. Ed.* **59**, 13021–13027 (2020).
- Zou, H., Rong, W., Wei, S., Ji, Y. & Duan, L. Regulating kinetics and thermodynamics of electrochemical nitrogen reduction with metal single-atom catalysts in a pressurized electrolyser. *Proc. Natl Acad. Sci. USA* **117**, 29462–29468 (2020).
- Zhai, G. Y. et al. Isoelectric Si heteroatoms as electron traps for N_2 fixation and activation. *Adv. Funct. Mater.* **30**, 2005779 (2020).
- Zhao, Y. et al. Identification of M-NH_2 - NH_2 intermediate and rate determining step for nitrogen reduction with bioinspired sulfur-bonded FeW catalyst. *Angew. Chem. Int. Ed.* **60**, 20331–20341 (2021).
- Gao, P. et al. Schottky barrier-induced surface electric field boosts universal reduction of NO_x^- in water to ammonia. *Angew. Chem. Int. Ed.* **60**, 20711–20716 (2021).
- Fang, Y. et al. Graphdiyne-induced iron vacancy for efficient nitrogen conversion. *Adv. Sci.* **9**, e2102721 (2022).
- Tang, C. & Qiao, S. Z. How to explore ambient electrocatalytic nitrogen reduction reliably and insightfully. *Chem. Soc. Rev.* **48**, 3166–3180 (2019).

11. Wang, Y. et al. Enhanced nitrate-to-ammonia activity on copper-nickel alloys via tuning of intermediate adsorption. *J. Am. Chem. Soc.* **142**, 5702–5708 (2020).
12. Gao, Q. et al. Breaking adsorption-energy scaling limitations of electrocatalytic nitrate reduction on intermetallic CuPd nanocubes by machine-learned insights. *Nat. Commun.* **13**, 2338 (2022).
13. Van Langevelde, P. H., Katsounaros, I. & Koper, M. T. M. Electrocatalytic nitrate reduction for sustainable ammonia production. *Joule* **5**, 290–294 (2021).
14. Zheng, X. C., Xue, Y. R., Zhang, C. & Li, Y. L. Controlled growth of multi-dimension interface for high selectivity ammonia production. *CCS Chem.* <https://doi.org/10.31635/ccschem.022.202202005> (2022).
15. Luan, X., Zheng, Z., Zhao, S., Xue, Y. & Li, Y. Controlled growth of the interface of CdWO₄/GDY for hydrogen energy conversion. *Adv. Funct. Mater.* **32**, 2202843 (2022).
16. Zhao, S., Zheng, Z., Qi, L., Xue, Y. & Li, Y. Controlled growth of donor-bridge-acceptor interface for high-performance ammonia production. *Small* **18**, e2107136 (2022).
17. Zheng, Z., Qi, L., Xue, Y. & Li, Y. Highly selective and durable of monodispersed metal atoms in ammonia production. *Nano Today* **43**, 101431 (2022).
18. Zhang, L. et al. Coordination of atomic Co-Pt coupling species at carbon defects as active sites for oxygen reduction reaction. *J. Am. Chem. Soc.* **140**, 10757–10763 (2018).
19. Liu, Y., Gao, Y., He, F., Xue, Y. & Li, Y. Controlled growth interface of charge transfer salts of Nickel-7,7,8,8-tetracyanoquinodimethane on surface of graphdiyne. *CCS Chem.* <https://doi.org/10.31635/ccschem.022.202202005> (2022).
20. Li, Z. et al. Titania-supported Ni₂P/Ni catalysts for selective solar-driven CO hydrogenation. *Adv. Mater.* **33**, e2103248 (2021).
21. Duan, Y. X. et al. Boosting production of HCOOH from CO₂ electroreduction via Bi/CeO_x. *Angew. Chem. Int. Ed.* **60**, 8798–8802 (2021).
22. Su, H., Soldatov, M. A., Roldugin, V. & Liu, Q. Platinum single-atom catalyst with self-adjustable valence state for large-current-density acidic water oxidation. *eScience* **2**, 102–109 (2022).
23. Rao, P. et al. Single atomic cobalt electrocatalyst for efficient oxygen reduction reaction. *eScience*. <https://doi.org/10.1016/j.esci.2022.05.004> (2022).
24. Chen, H., Zhang, J., Liu, X. & Liu, Z. Effect of gas-phase reaction on the CVD growth of graphene. *Acta Phys. -Chim. Sin.* **0**, 2101053–2101050 (2021).
25. Liu, C. et al. Nd³⁺-sensitized upconversion metal-organic frameworks for mitochondria-targeted amplified photodynamic therapy. *Angew. Chem. Int. Ed.* **59**, 2634–2638 (2020).
26. Gu, Z., Zhu, S., Yan, L., Zhao, F. & Zhao, Y. Graphene-based smart platforms for combined cancer therapy. *Adv. Mater.* **31**, e1800662 (2019).
27. Gao, Y. et al. Rhodium nanocrystals on porous graphdiyne for electrocatalytic hydrogen evolution from saline water. *Nat. Commun.* **13**, 5227 (2022).
28. Gao, Y., Xue, Y., He, F. & Li, Y. Controlled growth of a high selectivity interface for seawater electrolysis. *Proc. Natl Acad. Sci. USA* **119**, e2206946119 (2022).
29. Xu, H., Ma, Y., Chen, J., Zhang, W. X. & Yang, J. Electrocatalytic reduction of nitrate— a step towards a sustainable nitrogen cycle. *Chem. Soc. Rev.* **51**, 2710–2758 (2022).
30. Cao, L. M., Lu, D., Zhong, D. C. & Lu, T. B. Prussian blue analogues and their derived nanomaterials for electrocatalytic water splitting. *Coord. Chem. Rev.* **407**, 213156 (2020).
31. Rong, W. et al. Size-dependent activity and selectivity of atomic-level copper nanoclusters during CO/CO₂ electroreduction. *Angew. Chem. Int. Ed.* **60**, 466–472 (2021).
32. Li, G. et al. Architecture of graphdiyne nanoscale films. *Chem. Commun.* **46**, 3256–3258 (2010).
33. Jia, Z. et al. Synthesis and properties of 2D carbon-graphdiyne. *Acc. Chem. Res.* **50**, 2470–2478 (2017).
34. Huang, C. et al. Progress in research into 2D graphdiyne-based materials. *Chem. Rev.* **118**, 7744–7803 (2018).
35. Fang, Y., Liu, Y., Qi, L., Xue, Y. & Li, Y. 2D graphdiyne: an emerging carbon material. *Chem. Soc. Rev.* **51**, 2681–2709 (2022).
36. Zuo, Z. & Li, Y. Emerging electrochemical energy applications of graphdiyne. *Joule* **3**, 899–903 (2019).
37. Du, Y., Zhou, W., Gao, J., Pan, X. & Li, Y. Fundament and application of graphdiyne in electrochemical energy. *Acc. Chem. Res.* **53**, 459–469 (2020).
38. Xue, Y. et al. Anchoring zero valence single atoms of nickel and iron on graphdiyne for hydrogen evolution. *Nat. Commun.* **9**, 1460 (2018).
39. He, F. & Li, Y. Advances on theory and experiments of the energy applications in graphdiyne. *CCS Chem.* <https://doi.org/10.31635/ccschem.022.202202328> (2022).
40. Shen, H., Li, Y. & Li, Y. Self-assembly and tunable optical properties of intramolecular charge transfer molecules. *Aggregate* **1**, 57–68 (2020).
41. Yu, H. D. et al. Graphdiyne based metal atomic catalysts for synthesizing ammonia. *Natl Sci. Rev.* **8**, nwa213 (2021).
42. Hui, L. et al. Highly dispersed platinum chlorine atoms anchored on gold quantum dots for a highly efficient electrocatalyst. *J. Am. Chem. Soc.* **144**, 1921–1928 (2022).
43. An, J., Zhang, H., Qi, L., Li, G. & Li, Y. Self-expanding ion-transport channels on anodes for fast-charging lithium-ion batteries. *Angew. Chem. Int. Ed.* **61**, e202113313 (2022).
44. Hui, L. et al. Overall water splitting by graphdiyne-exfoliated and -sandwiched layered double-hydroxide nanosheet arrays. *Nat. Commun.* **9**, 5309 (2018).
45. Zheng, Z., Xue, Y. & Li, Y. A new carbon allotrope: graphdiyne. *Trends Chem.* **4**, 754–768 (2022).
46. Li, J. et al. Graphdiyne: a metal-free material as hole transfer layer to fabricate quantum dot-sensitized photocathodes for hydrogen production. *J. Am. Chem. Soc.* **138**, 3954–3957 (2016).
47. Zhao, Y. et al. Few-layer graphdiyne doped with sp-hybridized nitrogen atoms at acetylenic sites for oxygen reduction electrocatalysis. *Nat. Chem.* **10**, 924–931 (2018).
48. Xue, Y., Li, Y., Zhang, J., Liu, Z. & Zhao, Y. 2D graphdiyne materials: challenges and opportunities in energy field. *Sci. China Chem.* **61**, 765–786 (2018).
49. Xu, C. et al. Interpretation of rubidium-based perovskite recipes toward electronic passivation and ion-diffusion mitigation. *Adv. Mater.* **34**, e2109998 (2022).
50. Zhao, Y. et al. Stereodefined codoping of sp-N and S atoms in few-layer graphdiyne for oxygen evolution reaction. *J. Am. Chem. Soc.* **141**, 7240–7244 (2019).
51. Kong, Y. et al. Bridging the gap between reality and ideality of graphdiyne: the advances of synthetic methodology. *Chem* **6**, 1933–1951 (2020).
52. Gao, N. et al. Graphdiyne: a new carbon allotrope for electrochemiluminescence. *Angew. Chem. Int. Ed.* **61**, e202204485 (2022).
53. Guo, J. et al. Graphdiyne: structure of fluorescent quantum dots. *Angew. Chem. Int. Ed.* **59**, 16712–16716 (2020).
54. Zhang, S. et al. Graphdiyne: bridging SnO₂ and perovskite in planar solar cells. *Angew. Chem. Int. Ed.* **59**, 11573–11582 (2020).
55. Yang, Q. et al. Hydrogen-substituted graphdiyne ion tunnels directing concentration redistribution for commercial-grade dendrite-free zinc anodes. *Adv. Mater.* **32**, e2001755 (2020).
56. Fang, Y., Xue, Y., Hui, L., Yu, H. & Li, Y. Graphdiyne@Janus magnetite for photocatalytic nitrogen fixation. *Angew. Chem. Int. Ed.* **60**, 3170–3174 (2021).
57. Wei, H. et al. Mimicking efferent nerves using a graphdiyne-based artificial synapse with multiple ion diffusion dynamics. *Nat. Commun.* **12**, 1068 (2021).
58. Li, J. et al. Synthesis of wafer-scale ultrathin graphdiyne for flexible optoelectronic memory with over 256 storage levels. *Chem* **7**, 1284–1296 (2021).
59. Wen, J. et al. Direct charge trapping multilevel memory with graphdiyne/MoS₂ van der waals heterostructure. *Adv. Sci.* **8**, e2101417 (2021).
60. Yi, Y. et al. Highly potassiophilic graphdiyne skeletons decorated with Cu quantum dots enable dendrite-free potassium-metal anodes. *Adv. Mater.* **34**, e2202685 (2022).
61. Yang, Q. et al. Stabilizing interface pH by N-modified graphdiyne for dendrite-free and high-rate aqueous Zn-ion batteries. *Angew. Chem. Int. Ed.* **61**, e202112304 (2022).
62. Jia, Y. et al. Defect graphene as a trifunctional catalyst for electrochemical reactions. *Adv. Mater.* **28**, 9532–9538 (2016).
63. Zhang, L. et al. Beyond platinum: defects abundant CoP₃/Ni₂P heterostructure for hydrogen evolution electrocatalysis. *Small Sci.* **1**, 2000027 (2021).
64. Garcia-Segura, S., Lanzarini-Lopes, M., Hristovski, K. & Westerhoff, P. Electrocatalytic reduction of nitrate: fundamentals to full-scale water treatment applications. *Appl. Catal. B-Environ.* **236**, 546–568 (2018).
65. Chen, G. F. et al. Electrochemical reduction of nitrate to ammonia via direct eight-electron transfer using a copper-molecular solid catalyst. *Nat. Energy* **5**, 605–613 (2020).